



Surface-sediment dynamics in a dust source from spaceborne multispectral thermal infrared data

Itzhak Katra*, Nicholas Lancaster

Division of Earth and Ecosystem Sciences, Desert Research Institute, 2215 Raggio Parkway, Reno, NV 89512, United States

ARTICLE INFO

Article history:

Received 19 December 2007

Received in revised form 20 March 2008

Accepted 21 March 2008

Keywords:

Dust

Playa

Sediment

ASTER

Thermal infrared

Spectral analysis

ABSTRACT

This study utilized spaceborne multispectral thermal infrared (TIR) data to document spatial relationships of surface sediments over time in a modern depositional environment associated with dust emissions, Soda Lake playa, Mojave Desert, United States. The approach employed here involved time-series TIR data acquired from Advanced Spaceborne Thermal Emission and Reflection Radiometer (ASTER) and a linear spectral mixture analysis. An automated algorithm was applied to derive emissivity image endmembers. Evaluation of the chosen endmembers revealed that they can be categorized into five major spectra classes based on diagnostic absorption features. Each spectrum has been identified in relation to mineral abundance and soil arrangement that are common in playa settings: A, “clayey silt-rich crust”; B, “intermediate-salt crust”; C, “quartz-rich deposit”; D, “salt-rich rough crust”; E, “sulfate-rich crust”. Spectral classes A–B–C–D yielded the lowest RMS errors (0–0.025) over time in the iterative deconvolution algorithm between the measured and modeled spectra. The produced fractional abundance images show high areal concentrations for clayey silt-rich crust, salt-rich rough crust, and quartz-rich deposit, as the first surficial mapping of Soda Lake. Significant changes in the spatial relationships of the major surface sediments in Soda Lake were observed after a flooding event (2005) and a relatively dry period (2006). The approach utilized in this study can be advantageous for continuous monitoring of environments characterized by a small area and a complex surface, which may enable a better understanding of their responses to climate changes and potential for dust emissions.

© 2008 Elsevier Inc. All rights reserved.

1. Introduction

Desert dust has many impacts on climate, ecosystems, and humans (Goudie & Middleton, 2006). The most productive areas for dust appear to be modern and ancient sediment-depositional environments located mainly in arid regions (e.g., Gillette, 1999; Prospero et al., 2002; Washington et al., 2006). One type of dust source is playa (dry lake). An episodic influx of surface water introduces clastic materials to the ephemeral lake, while evaporation of near-surface brines leads to accumulation of chemical constituents on and within the near-surface (Eugster & Hardie, 1978; Rosen 1994). The sedimentation processes in playas result in dynamic surfaces that are sometimes vulnerable to wind erosion (Reheis, 2006; Reynolds et al., 2007). Continued advances in understanding dust sources and modeling dust emissions depend on spatially-detailed quantification of their surface sediments over time.

Remote sensing data in the visible-near infrared (VNIR) and shortwave infrared (SWIR) wavelength regions have been used with various techniques to study sediments in playa environments located in Africa (Bryant, 1996; Millington et al., 1989), Asia (Rezaei & Saghafi,

2006), North America (Crowley, 1993), and South America (Kampf & Tyler, 2006). The use of these parts of the electromagnetic spectrum, however, may be limited due to the inability to accurately distinguish spectral signatures of many silicate-rich minerals common in playa settings (Blount et al., 1990; Ramsey et al., 1999). Moreover, Crowley (1993) noted that several important evaporites involved in playas, including thenardite and anhydrite, exhibit generally featureless spectra in the SWIR region. Silicate, evaporite and other common minerals in playa settings do exhibit diagnostic spectral features in the TIR spectral range that simplify their remote discrimination. Crowley and Hook (1996) have utilized airborne multispectral TIR (8–12 μm) data acquired from Thermal Infrared Multispectral Scanner (TIMS) at a single flight to successfully map a variety of surface crusts containing abundant evaporite and silicate minerals in Death Valley salt pan, California, employing supervised classification based vector-angle comparison between known spectra and image spectra. Airborne data, however, are not cost-effective for multitemporal observations. Data with similar TIR spectral capabilities are globally available from the satellite instrument Advanced Spaceborne Thermal Emission and Reflection Radiometer (ASTER), which is aboard the Terra platform as part of NASA's Earth Observing System (EOS). Since ASTER was launched (December 1999), its multispectral TIR data have been used to identify surface minerals mainly within the context of lithology and

* Corresponding author. Tel.: +1 775 6737610.

E-mail addresses: katra_ik@yahoo.com, itzhak.katra@dri.edu (I. Katra).

natural resources (e.g., Rowan & Mars, 2003; Vaughan et al., 2005). No attempt has been made to use spaceborne multispectral TIR data to study sediments in dynamic landforms as playas.

The objective of this study is to utilize ASTER TIR data to identify the surface sediments in a modern playa, Soda Lake (CA), associated with dust emissions, and to illustrate their spatial distribution over time. To this end, a time-series of ASTER TIR data was first evaluated and then spectrally analyzed. The nature of the TIR energy emitted from surface materials and the spatial mixture at a scale below that of a pixel motivated the use of a spectral deconvolution to retrieve sub-pixel information related to areal abundances of surface materials. The methods and the obtained results of the data processing are described in Sections 5 and 6. The fractional abundance images are discussed in Section 7.

2. Theoretical framework

2.1. TIR spectral features

Various clastic and chemical minerals encountered within playas exhibit wavelength-dependent molecular absorption features in the 8–12 μm region. A mineral spectrum is usually characterized by spectral emissivity minima caused by fundamental vibrational modes in the crystal lattice of the mineral. Silicate-rich minerals such as quartz and montmorillonite show a broad asymmetric band which has emissivity

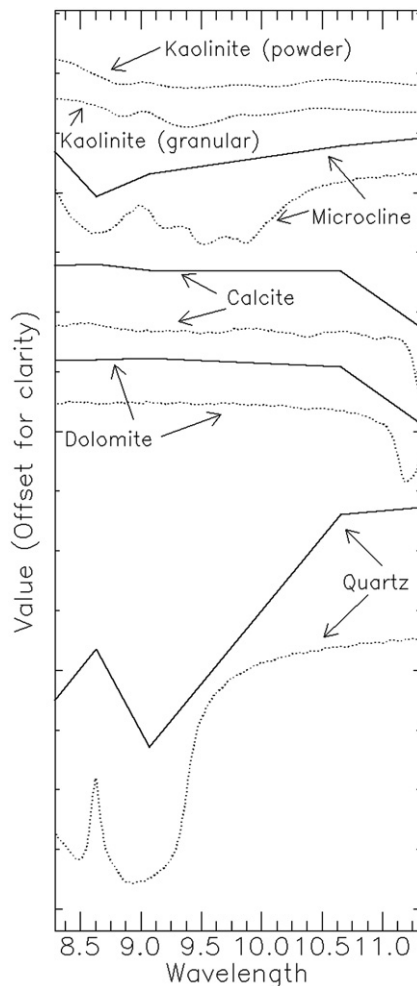


Fig. 1. Emissivity spectra of a number of minerals plotted in laboratory (dashed lines) and the five ASTER channels resolutions. Laboratory spectra from ASU thermal emission spectral library (Christensen et al., 2000). Spectra are offset on the vertical axis for clarity at 0.10 segments.

minima between approximately 9 and 10 μm (Fig. 1) due to the Si–O stretching modes (e.g., Hunt, 1980). In the molecular unit of sulfate (gypsum, anhydrite), the spectral features at 8–9 μm arise from oscillations of the S–O bond structure (e.g., Clark, 1999). A uniform electrostatic charge across the crystal of chlorides such as thenardite produces a relatively broad absorption band around the 8–9 μm wavelengths. For carbonate minerals, spectral features result primarily from fundamental vibrations of the C–O bonds in the carbonate anions (CO_3^{2-}), but dolomite, in which the mineral structure alternates layers of calcium and magnesium, may show spectral absorption in shorter wavelengths (11 μm) than that of the calcite (e.g., Lane & Christensen, 1997). Such distinctive spectral features permit the minerals to be identified in multispectral TIR data. Nonetheless, some spectral features may be undersampled and become obscured in the convolution to a sensor channels. For example, the calcite (CaCO_3) emissivity spectrum is severely degraded in the ASTER filtered spectrum (Fig. 1) as its band is much narrower than the ASTER band and it is likely to be very shallow because of the fine grain size (see below). In addition, the lack of an ASTER channel in the 10 μm region (ozone absorption band) affects the discrimination of some minerals, especially mafic rock-forming minerals such as feldspars/microcline (Fig. 1). Previous studies have addressed the issue of energy scattering and the effect of particle size on TIR spectra (e.g., Clark, 1999; Hunt, 1980; Salisbury & Wald, 1992). As the grain size decreases, the spectral feature depth also decreases (i.e., higher emissivity) due to differences in porosity and optical thickness, and their effect on volume scattering (see kaolinite in Fig. 1). Significant changes in the position of the spectral features may occur for non-solid and/or fine-grained (<40 μm) particles (e.g., Salisbury & Wald, 1992). Minerologically, a large portion of independent surface grains in playa settings are below that size. In practice, however, evaporation of solute-rich groundwater commonly results on durable crusts in the playa surface that consist of evaporite minerals or mixture of evaporite and silt-clay sediments (Eugster & Hardie, 1978; Rosen, 1994), which increase the effective radiating diameter.

2.2. TIR deconvolution

The spectrum of a single pixel in a satellite image space is typically a mixture of more than one surface material. It has been demonstrated that the thermal infrared spectrum of a mixed surface may be closely modeled using a linear combination of a few spectrally unique components (endmembers) weighted by the areal concentration of each endmember (Gillespie, 1992; Ramsey & Christensen, 1998; Ramsey et al., 1999). The fundamental principle of spectral mixture analysis is that the endmembers combine in the composite spectrum in proportion to their areal fractions, allowing a determination of the best fit endmember percentages for a given mixture spectrum (Adams & Gillespie, 2006; Gillespie, 1992; Ramsey & Christensen, 1998):

$$\varepsilon(\lambda)_i = \sum_{i=1}^n f_i \varepsilon(\lambda)_i + r(\lambda)_i \quad (1)$$

where ε is the radiance value of endmember i for a specific channel (λ), f_i is the fraction of the endmember, n is the number of endmembers, and r is the residual error. The modeled fractions of the endmembers are constrained by:

$$\sum_{i=1}^n f_i = 1.0 \quad (2)$$

Residuals for all channels (m) can be combined into a root-mean squared (RMS) error, to assess the model fit:

$$\text{RMS} = \sqrt{\frac{\sum_{j=1}^m r(\lambda)_i^2}{m}} \quad (3)$$

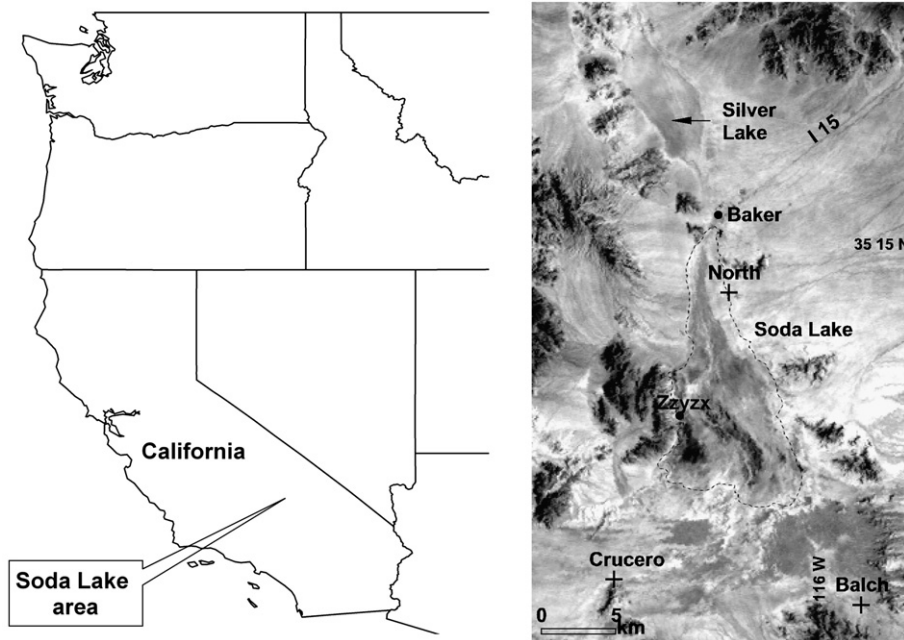


Fig. 2. Location map of the study site and ASTER TIR image (channel 10, May 2004) of the greater Soda Lake area. The black dashed region denotes the playa contour (after Brown, 1989), representing the area analyzed in detail. Balch, North, and Crucero are meteorological stations (CLIM-MET) of U.S. Geological Survey (<http://esp.cr.usgs.gov/info/sw/clim-met>).

Different solutions may be used to solve a linear mixture model in which a constrained least-squares solution is the most frequently one due to its simplicity. Nonetheless, the mixing equation is mathematically sensitive when the endmember vectors are too similar as the fraction values fluctuate sensitively in response to small changes in channel DNs (Adams & Gillespie, 2006). The number and identity of endmembers depend upon the nature of the scene, but also the spectral resolution, the number of bands, and the spatial scale (Gillespie, 1992). The use of TIR emissivity-separated data may simplify the model as only one unknown parameter (emissivity) per component in a pixel is determined, while in TIR radiance data, there are two unknowns (temperature and emissivity).

3. Soda (dry) Lake playa

3.1. Evolution, geology and hydrology

Soda Lake is located in the northeast edge of the Mojave River, Mojave Desert, California (Fig. 2). The Mojave River crosses several tectonic basins bounded by northwest–southeast oriented right-lateral strike-slip faults (e.g., Brown, 1989). During the Pleistocene the River filled these basins with fluvial, deltaic, playa, and lacustrine

deposits to form the late Pleistocene lakes Harper Lake, Lake Manix, and Lake Mojave (Enzel et al., 2003). A transition to a drier climatic regime resulted in the total drying of Lake Mojave by ca. 8.7 ka, with playa conditions dominating Soda Lake and Silver lake basins following this event (Wells et al., 2003). At present time, Soda Lake occupies a topographic low (+280 m a.s.l.) with an area of approximately 95 km². The playa is surrounded by large bedrock outcrops (Soda Mountains, Little Cowhole and Cowhole Mountains) and associated alluvial fan complexes. These outcrops are composed of early Precambrian metamorphic, late Precambrian and Paleozoic sedimentary rocks (sandstone, shale, conglomerates, and carbonates), coarse-grained Mesozoic granites, granodiorites and diorites and Cenozoic volcanic rocks. South of Soda Lake there are extensive aeolian sand sheets and fluvial sediments derived from the broad fan complex related to the terminus of the Mojave River (Brown, 1989; Enzel et al., 2003). Brown (1989) showed that the upper 0.5 m-layer in the center of the playa, north, and southeast, contains mainly silt and clay, while this layer in the north and the southwestern is sandy. The Soda Lake area experiences hyperarid climatic conditions with less than 100 mm of mean annual precipitation and estimated evaporation of 200–250 mm/year. Measurements conducted by the U.S. Geological Survey from 1956 to 1985 (<http://waterdata.usgs.gov/nwis>) showed



Fig. 3. Photographs of Soda Lake playa in (A) flooding on February 20, 2005, following heavy precipitation event in January 2005 (see data in Fig. 5), and (B) blowing of evaporite-mineral dust event on February 6, 2001. The photographs taken by Robert Fulton, California Desert Consortium, Baker, CA.

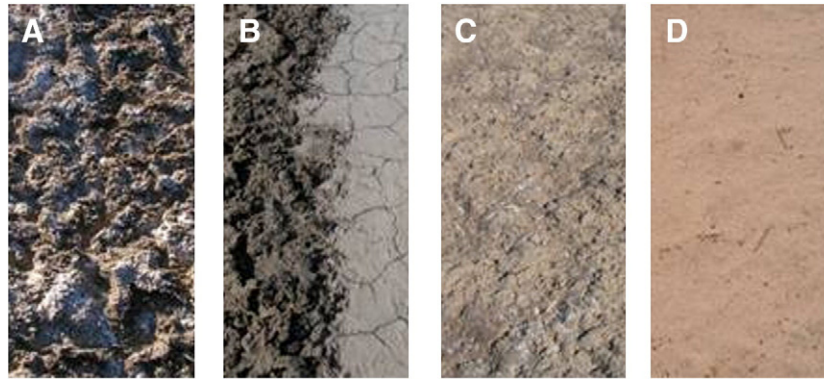


Fig. 4. Surface types observed in various locations in Soda Lake on April 13, 2007. (A) Dry, porous crust-surface with microrelief of numerous centimeters, composed mainly of massive halite and thenardite along with quartz, feldspar, and mica. (B) Transition between crusted soils, dry, porous surface (left) and dry, hard surface. (C) Clayey silt crust composed mainly of muscovite, phlogopite, biotite, illite, and quartz. (D) Quartz-rich deposit.

that the groundwater levels beneath the playa are likely to vary in space and time. Along the western margin, the groundwater table is at or near the surface of the playa, deepening toward the east and north to about 5 m and lower (>20 m) beneath the alluvial fans on the eastern side of the basin. The major brine type is $\text{Na-CO}_3\text{-Cl-SO}_4$ (Eugster & Hardie, 1978), indicating precipitation of Na-rich minerals in the playa.

3.2. Surface characteristics

Soda Lake has a relatively flat surface, where most of it is vegetation-free, or has a distinct vegetation association. Extreme southerly displacement of the Jet Stream over the eastern North Pacific usually causes the Mojave River to flood the playa surface (e.g., Brown, 1989) (Fig. 3A), but the subsequent desiccation result development of efflorescent salts that are vulnerable to wind erosion (Fig. 3B). Most of the dust is emitted from the greater Soda Lake area (playa and alluvial fans) during the late winter and spring. Reheis and Kihl (1995) and Reheis (2006) reported on variations in fluxes of silt-clay, soluble-salt, and carbonate related to climatic factors, in particular, seasonally and yearly precipitation. Large areas in the

western margin are covered in salts, while in the eastern part of the playa surface tends to be hard packed and lack efflorescent salt (Reynolds et al., 2007). Kerr and Langer (1965) have studied samples from representative Mojave playas. The sample taken from Soda Lake was a soft, porous, puffy crust-type composed of common rock-derived minerals (quartz, microcline, muscovite, biotite) and chemical minerals (halite, thenardite, anhydrite). Some current surface types in Soda Lake and the associated minerals from X-ray diffraction analysis are presented in Fig. 4. The Soda Lake surface, however, has never been mapped.

4. ASTER TIR data set

ASTER records spectral radiance in five TIR channels, producing day or night time scenes (~60×60 km) with a spatial resolution of 90 m/pixel and a $\text{NE}\Delta T < 0.3 \text{ K}$ (Yamaguchi et al., 1998). The five channels (#10–14) are centered on 8.29, 8.63, 9.08, 10.66, and 11.32 μm , respectively. For this study, we acquired Level-2 (L2) surface-leaving radiance (AST_09T) and the emissivity (AST_05) products from the Land Processes Distributed Active Archive Center (LP DAAC) at the U.S. Geological Survey Center for Earth Resources

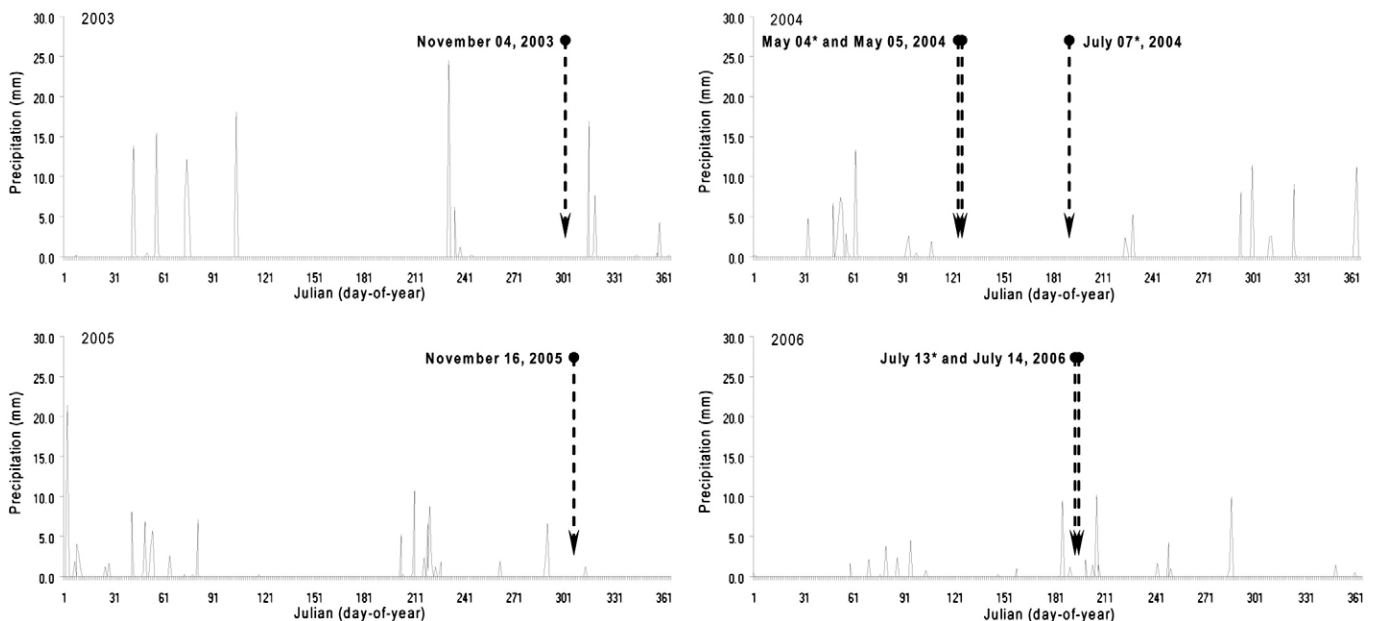


Fig. 5. Summary of the ASTER TIR scenes on the background of average daily precipitation (mm) received in the CLIM-MET stations around Soda Lake (see Fig. 2) in each year (2003–2006). Night-time scenes are noted by asterisks.

Observation and Science (EROS) (<http://LPDAAC.usgs.gov>). AST_09T product, created from the Level-1B, has been radiometrically, geometrically, and atmospherically corrected. The L1B is produced by applying the radiometric calibration and geometric correction coefficients to the Level-1A data, resulting in an absolute accuracy of 2% and a relative accuracy of 1% (Yamaguchi et al., 1998). The AST_05 product is derived from the AST_09T data using the Temperature Emissivity Separation algorithm developed by Gillespie et al. (1998), which accounts for both the spectral contrast and downwelling atmospheric irradiance. As L1B data are processed on demand, the subsequent L2 products have the same atmospheric correction. Scenes were selected from the ASTER data available using the USGS Global Visualization Viewer website (<http://glovis.usgs.gov>). An attempt was made to choose scenes recorded at different time intervals, based on overall quality, low cloud cover (>3%) and clear sky above the Soda Lake. Seven scenes, four days (~18:30 UTC) and three night time (~05:50 UTC) data were selected from the ASTER TIR database, spanning from November 2003 to July 2006 (Fig. 5). The dates correspond to time spans between which precipitation occurred during these years in that area, in which the upper most layer of the playa was relatively dry.

5. TIR data evaluation

The first step of the data analysis process (Fig. 6) was evaluation of the TIR data and the compositional emissivity spectra of Soda Lake surface using a decorrelation stretching (DCS) technique. The DCS, explained in detail by Gillespie et al. (1986), is a transformation of the original data that removes the high correlation commonly found in TIR multispectral data sets and allows the thermal and emissivity variations to be distinguished visually. The combination of the channels 14 (R), 12 (G) and 10 (B) have been found to be particularly effective by users of ASTER TIR data (e.g., Rowan & Mars, 2003). A first DCS was performed on the AST_09T image set of the greater Soda Lake area. Summarized results in Fig. 7 show variations in the playa surface that stand out on a relatively steady background. A second DCS was

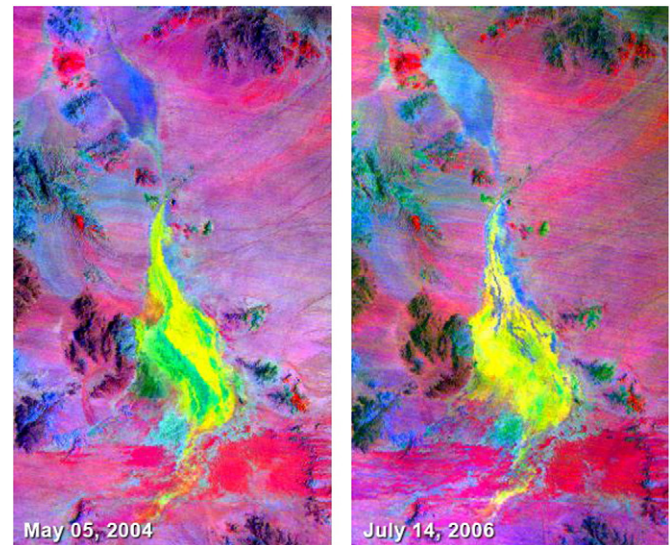


Fig. 7. DCS of ASTER TIR radiance of the greater Soda Lake area (see Fig. 2). TIR DCS channels 14, 12, and 10 (wavelengths 11.32, 9.08, and 8.29 μm) are displayed as RGB, respectively. Typically, magenta–red is evidence of silica-rich materials, and the yellow–green–blue tones may indicate chemical products as carbonate and sulfate. Note that the playa surface changes with time, while the features surrounding have the same color compositions in both images. (For interpretation of the references to color in this figure legend, the reader is referred to the web version of this article.)

performed for the emissivity data set, considering only the playa surface (Fig. 8). The results of this transformation show clear variations in color and composition over time, indicating spatial and temporal variations in surface materials throughout the playa. No attempt was done in this step to identify and quantify the surface sediments. However, the similar color composition observed for consecutive night- and day-time images (May-4 and May-5 2004 and July-13 and July-14 2006) was well expected due to the very short time of several hours between such paired images and the lack of precipitation events (Fig. 5). The DCS transformation results (Figs. 7 and 8) support the basic assumption regarding surface-sediment variations in space and time at Soda Lake, suggesting that the TIR data set may be useful for further spectral analysis.

6. Spectral mixture analysis

6.1. Image endmembers

Endmember spectra are extreme pixels in the scene that they mix together to explain most of the spectral variance in the image space. The selection of endmembers therefore is a key to generate physically-meaningful fraction images that can be interpreted as surface-material abundance maps. Image endmembers extracted from pixel spectra do not need to be calibrated to the image and can be obtained from the image space. The time-series emissivity data set of the unstudied surface of Soda Lake was a trigger in this study to apply an automated algorithm for endmembers selection. Spectral endmembers were derived by the Sequential Maximum Angle Convex Cone (SMACC) (Gruninger et al., 2004). In this algorithm, extreme points are used to determine a convex cone, which defines the first endmember. A constrained oblique projection is then applied to the existing cone to derive the next endmember. The algorithm was run for each emissivity image of the Soda Lake surface only, until it found endmember already accounted for in the group of the predecessor endmembers. Up to five endmembers (#1–5) with different spectral characteristics were selected by the SMACC for each five-channel multispectral emissivity image. Evaluation of these endmembers revealed that they can be categorized into five different classes (A–E)

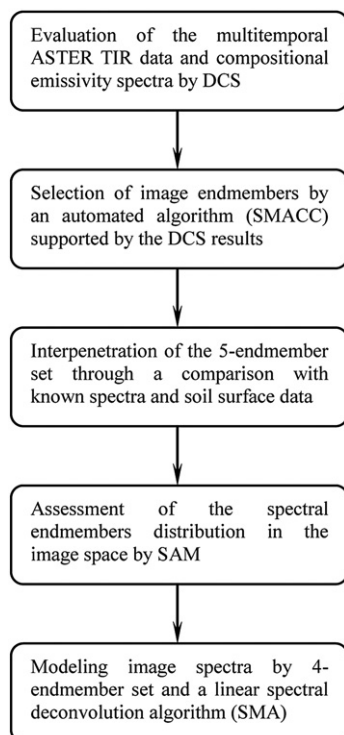


Fig. 6. Flow chart illustrating the data analysis process.

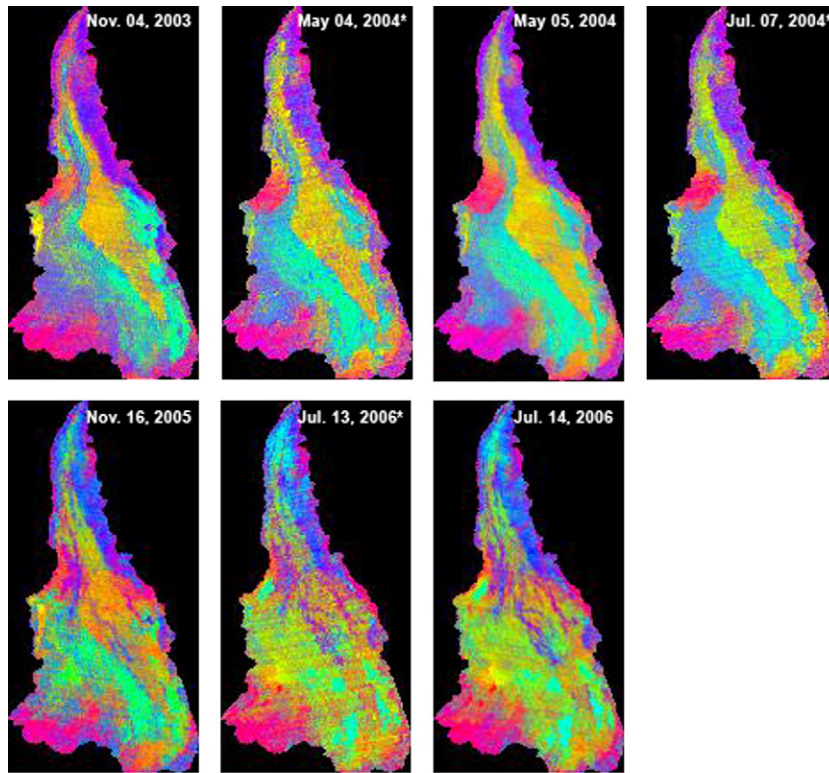


Fig. 8. DCS of ASTER emissivity images of the Soda Lake surface (see Fig. 2). Emissivity DCS channels 14, 12, and 10 (wavelengths 11.32, 9.08, and 8.29 μm) are displayed as RGB, respectively. Night-time images are noted by asterisks. Note the similarity in the color patterns between consecutive night and day images. (For interpretation of the references to color in this figure legend, the reader is referred to the web version of this article.)

based on their emissivity spectra (Fig. 9). Most of the curves show emissivity lows, approximately in 8.63 (class E), 9.08 (classes A and C), and 10.66 μm (class B), but there is also a relatively smooth curve (class D). This classification may be supported in a certain manner by the locations of the endmembers in the image space, which calculated by the SMACC model. The endmembers of classes A, B, C, and D were located in compositionally distinct areas that are associated with abundance of blue, green, magenta, and yellow, respectively, in the DCS images (Fig. 8), while endmembers of class E were located at

blue–magenta pixels. The endmembers in each class were averaged to create an endmember set (Fig. 10) for the spectral unmixing.

6.2. Endmember set

The spectral classes in Fig. 10 are assumed to represent major surface materials in Soda Lake. The image spectra can be interpreted simultaneously through a comparison with known spectra and a prior knowledge of the remotely sensed area. However, it is realistic to

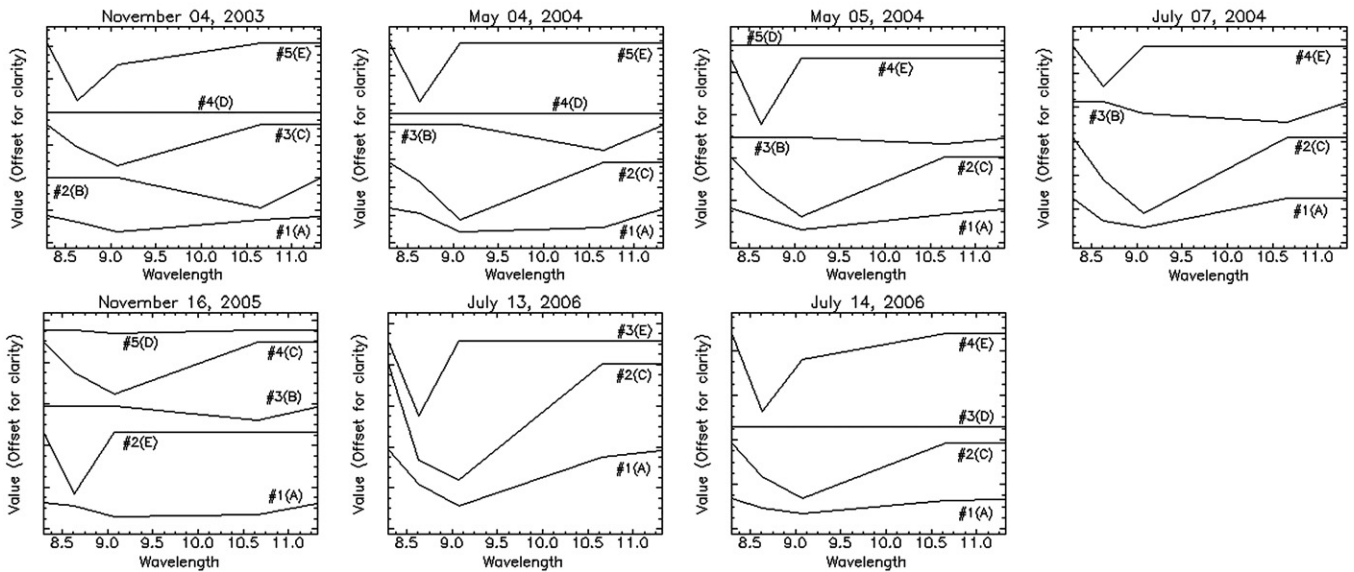


Fig. 9. Spectral image endmembers derived by SMACC for each emissivity image. The spectra are offset for clarity, and normalized to compare absorption features using continuum removal curve. The endmember in each plot are shown with respect to the model reproduce order (#1–5). Each endmember was classified (A to E) based on its spectral features, starting from November 2003.

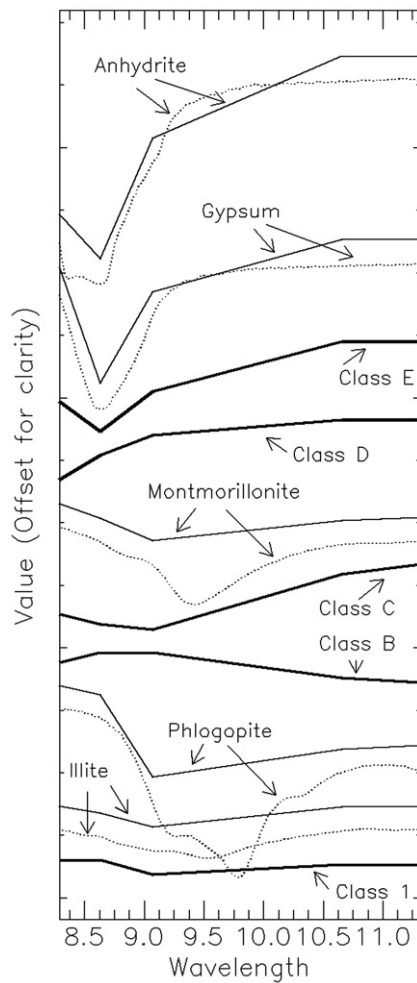


Fig. 10. Spectral library of surface materials in Soda Lake (classes A–E) along with some representative spectra of minerals at ASTER and laboratory (ASU thermal emission spectral library) resolutions.

define image spectra in terms of surface-sediment type (major mineral and soil arrangement) rather than specific minerals due to the mineralogic mixture at any spatial scale in remote sensing data. The emissivity spectrum of class A has low-contrast with a weak spectral feature near the 9.08 μm , similar to the curve of some phyllosilicate minerals laboratory spectra, for example, illite/muscovite (compound alteration), phlogopite, and biotite, which mainly contain Si, K, Al and Mg, and associated with weathering of granites, metamorphic limestones and dolomites rocks, typical of western and eastern Soda Lake (e.g., Brown, 1989). Illite, however, could be derived also from alteration of K-feldspars or recrystallization of smectites. Abundance of silt may form a crusty surface that usually varies in salt content, color, and micro-topography (see Fig. 4B, C) due to variations in sediment deposition. The emissivity curve of class B has an unusual shape with a minimum at 10.66 μm that does not fit a spectrum of a pure mineral. A similar spectrum, however, was shown by Crowley and Hook (1996) for massive halite (NaCl) with some mirabilite ($\text{Na}_2\text{SO}_4 \cdot 10\text{H}_2\text{O}$) of smooth crusts on floodplains in the Death Valley. The crystallization of these minerals associated with evaporation of very saline (Na– SO_4 –Cl brine types) and/or shallow groundwater. It can be linked to intermediate level of efflorescent salt crust development that occurs in desiccation events (Eugster & Hardie, 1978; Reynolds et al., 2007). Spectrum C exhibits a relatively strong absorption feature at 9.08 μm , indicating that quartz is an important constituent. Even though the convolution of quartz lab spectra to ASTER shows the characteristic doublet feature (Fig. 1), this is not

always seen in practice with ASTER emissivity spectra (Rowan et al., 2005). The quartz could be mixed with other silicate minerals such as montmorillonite ($[\text{Na},\text{Ca}]_{0.3}[\text{Al},\text{Mg}]_2\text{Si}_4\text{O}_{10}[\text{OH}]_2 \cdot n\text{H}_2\text{O}$), which is a reaction product of weathering volcanic rocks in a dry environment. The sand sheets located south to the playa and the alluvial fans located at the western and eastern margins (Figs. 2 and 7) are source areas for such sediment type (Fig. 4D) deposited in the playa by aeolian activity and surface water flows. In class D, a downward slope toward the shorter wavelengths of the emissivity spectra points to sulfate, for example, trona ($\text{NaHCO}_3 \cdot \text{Na}_2\text{CO}_3 \cdot 2\text{H}_2\text{O}$) and thenardite (Na_2SO_4). Similar emissivity spectra with Na-rich salts were demonstrated by Crowley and Hook (1996) in a crust sample which consists of thenardite, halite, dolomite, quartz, and muscovite. It can be linked to dehydration of surface with efflorescent salt that forms a dry, porous and salt-rich (rough) crust (Kerr & Langer, 1965; Reynolds et al., 2007) as shown in Fig. 4A. Spectrum E corresponds to spectra of Ca-sulfate salt minerals, in particular, pure gypsum ($\text{CaSO}_4 \cdot 2\text{H}_2\text{O}$) and anhydrite (CaSO_4) minerals. The gypsum is crystallized initially in areas with near-surface brines of Na–(Ca)–Cl composition. The anhydrite may not be formed by direct precipitation from the brine but through interaction of interstitial brine with sediments (Eugster & Hardie, 1978). These sulfates, however, occur usually as a minor constituent in a silty mixture surface. In this light, the spectra classes A to E were defined as “clayey silt-rich crust” (hard or soft), “intermediate-salt crust”, “quartz-rich deposit”, “salt-rich rough crust”, and “sulfate-rich crust”, respectively.

6.3. Preliminary classification

A Spectral Angle Mapper (SAM) classification was derived to assess the spectral classes (A–E, Fig. 10) distribution before the spectral unmixing. SAM compares the angle between a reference spectrum vector and each pixel vector in n -dimensional space, where smaller angles represent closer matches to the reference spectrum and pixels further away than the specified maximum angle threshold in radians are not classified (Kruse et al., 1993). From Table 1, it appears that the spectral classes A (clayey silt-rich crust) and D (salt-rich rough crust) have a high cover percentage over time, in which the value of spectrum A or D is always the highest among the classes. Class B (intermediate-salt crust) shows a higher value (16.8%) compared to class D (10.8%) in November 2003, but demonstrates a trend of decreasing cover percentage towards November 2005, including values of zero in July 2006. Class C (quartz-rich deposit) appears in all the dates with maximum of cover percentage in July 2004 and July 2006. Class E characterized by low values of less than 1% in most cases. The SAM results reveal that the endmembers A, C, and D play an important role in the image space, whereas endmember E (sulfate-rich crust) is not significant in terms of cover percentage over time. These distinctions were taken into consideration in the following step.

6.4. Modeling image spectra

The linear retrieval (spectral deconvolution) algorithm utilized in this study was demonstrated by Ramsey and Christensen (1998). It has

Table 1

Spectral classes (A–E) distribution (%) in the five-channel emissivity images of Soda Lake derived from Spectral Angle Mapper classification (threshold angle of 0.05 rad)

	Nov. 04 2003	May 04* 2004	May 05 2004	Jul.07* 2004	Nov. 05 2005	Jul.13* 2006	Jul.14 2006
A	65.0	47.4	55.4	40.4	60.8	27.2	22.9
B	16.8	4.9	6.1	3.5	0.7	0.0	0.0
C	7.2	11.8	11.2	15.6	6.5	19.0	34.6
D	10.8	35.9	27.3	40.4	31.8	53.3	41.9
E	0.2	0.1	0.0	0.1	0.2	0.5	0.6

Night-time images are noted by asterisks.

been used successfully in earth and planetary sciences for modeling fractional areal extent of endmembers and identifying individual surface materials within a single pixel (Bandfield, 2002; Michalski et al., 2004; Ramsey et al., 1999; and others). The algorithm employs a numerical chi-squares minimization technique with two main constraints. First, if one or more of the final values is negative (assuming no physical meaning), it is presumed that the endmember corresponding to that value is not present in the mixed spectrum and is therefore removed. In image format, this can be indicated as an area of potentially unmodeled endmember. A second constraint placed on the algorithm is that the element of the column vector must sum to unity. The unity condition produces fractional percentages which sum to 100% rather than a renormalization of the fractions as a final step. In this algorithm, the linear deconvolution of n -band data is limited to n possible endmembers, i.e. up to five endmembers in modeling ASTER TIR scenes. A library of four surface-material endmembers and one blackbody endmember (emissivity=1.0) was used to deconvolve the emissivity images. The incorporation of a blackbody component into the deconvolution routine allows for differences among the spectral contrast of the library endmembers (Michalski et al., 2004). The algorithm was run more than once, with different emissivity spectra combinations A–E (Fig. 10), to fit minimum values of RMS errors. The spectral combination of A–B–C–D yielded the best model fit in the spectral unmixing. These spectral classes were associated with the

highest values in most cases in the SAM results (Table 1), and with the color abundances in the DCS images (Fig. 8). The output of the algorithm consists of image layers for each of these endmembers with pixel values equal to the fractional abundance (in percentages) of that endmember, and RMS error image of the difference (0–1) between the measured and modeled spectrum. Fig. 11 shows fraction image sets for three representative dates: November 2003, November 2005, and July 2006. RMS errors ranged from zero to a maximum of 2.5% in emissivity for the entire set, having no correlation with any of the spectral classes. To illustrate the spatial relationships of the surface sediments in the entire set, the fraction images of each date were displayed in RGB format (Fig. 12). In these images, abundances of red, green, and blue, are associated with high percentage fraction of the spectral classes C, A, and D, respectively. Pixels with color composition, for example, blue–green tones, indicate that more than one spectrum is dominating them, but their proportion in each image space is relatively small.

7. Fraction images review

Figs. 11 and 12 represent the first mapping of Soda Lake playa. The clastic–evaporite mixture that characterizes most of the surface types may be seen in each fraction image (Fig. 11). However, it is possible to distinguish high areal concentrations among clayey silt-rich crust

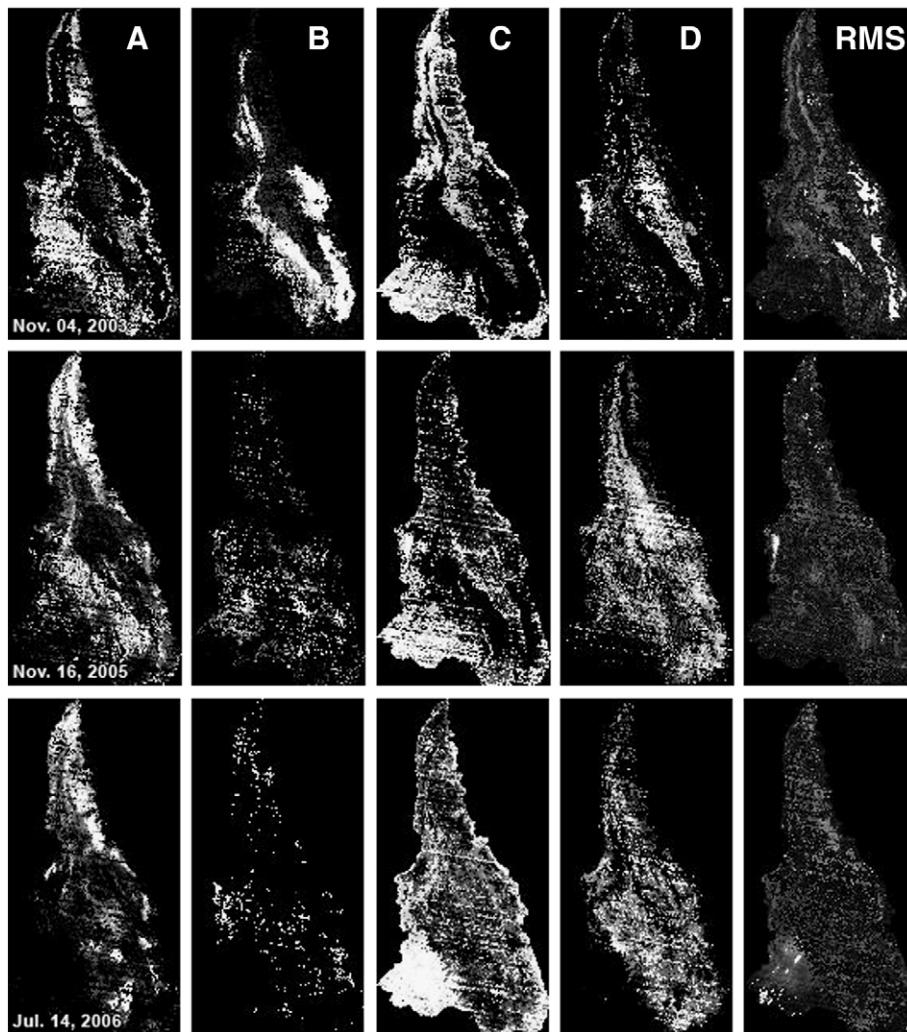


Fig. 11. Fractional abundance images for spectra endmembers A to D retrieved from ASTER emissivity spectral deconvolution for representative dates: November 2003 (upper row), November 2005, July 2006 (lower row). RMS errors: 0–0.025, 0–0.012, and 0–0.014, respectively. Endmembers areal concentrations are from 20% to 100%, where higher values are associated with white pixels. Classes A to D represent “clayey silt-rich crust”, “intermediate-salt crust”, “silicate-rich deposit”, and “salt-rich rough crust”, respectively (see text).

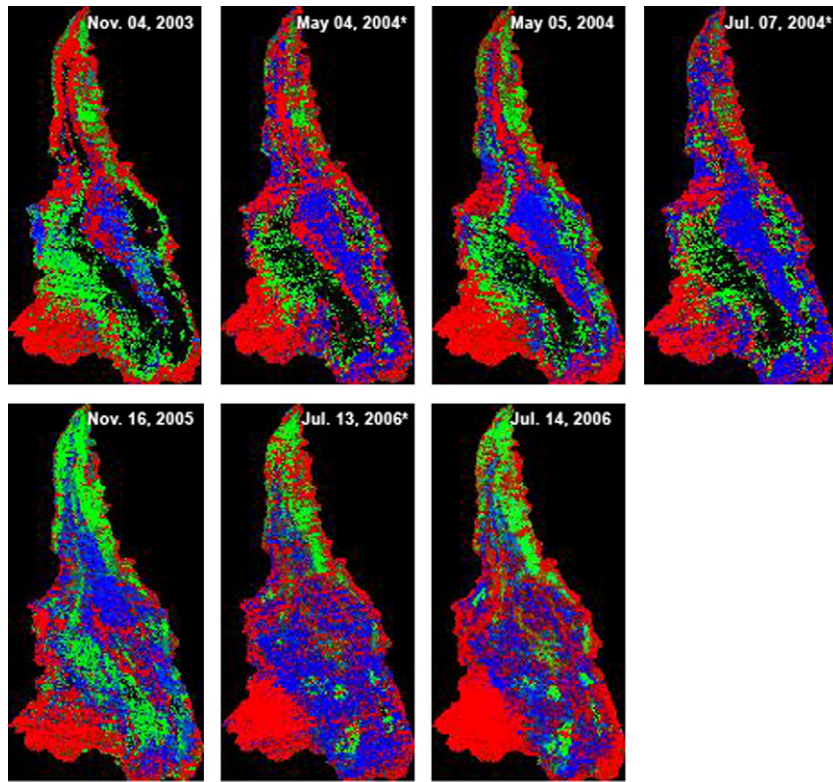


Fig. 12. Illustration of spatial relationships among selected surface sediments in Soda Lake over time. Abundance of red, green, and blue, are associated with higher values within the range 20–100% of “quartz-rich deposit”, “clayey silt-rich crust”, and “salt-rich rough crust”, respectively (see text). Black pixels within the playa contour are closely linked to “intermediate-salt crust” (class B in Fig. 11). (For interpretation of the references to color in this figure legend, the reader is referred to the web version of this article.)

(green), salt-rich rough crust (blue), and quartz-rich deposit (red), which stand out clearly in Fig. 12, suggesting that overall the selected spectral endmembers used to model the image spectra fit the model of Soda Lake surface over time very well. The surface-sediment types observed at Soda Lake playa appear to be common for wet playas in the southwestern United States (e.g., Neal, 1968; Reynolds et al., 2007). The main concentration areas of clayey-silt, salt, and quartz deposits in the playa may be supported in a certain manner by the qualitative description of Reynolds et al. (2007) and by the sedimentologic measurements of Brown (1989) (see Section 3).

Relatively minor changes are seen in the first four images that span eight months (November 2003 to July 2004), in contrast to significant changes in November 2005 and July 2006. The similarity in color abundances for consecutive night- and day-time images (May 2004 and July 2006), however, was anticipated. At the observed spatial and temporal scales, the minor changes until July 2004 can be related to the series of rain events that occurred at that time (Fig. 5), and as a consequence stabilizing in the hydrologic and the geomorphic processes. The most distinguishing and effective factor affecting modern depositional environment is flooding. Such events were documented in Soda Lake after a heavy rainfall (see data in Fig. 5) during late August 2003 and again in January–February 2005 (Fig. 3A). The significant rearrangement of the soil surface observed in November 2005, although it does not represent the playa surface immediately after the inundation and desiccation, can be related to the flooding of 2005. Massive quantities of fine-grained sediments were apparently transported by the Mojave River and deposited throughout the playa. This may explain the higher concentration of clayey silt-rich materials at the northern part of the playa in 2005 and 2006 compared to 2004. The inundation and the subsequent drying produced widespread surfaces rich in efflorescent salts that were probably eroded by wind in the period thereafter (Reheis, 2006; Reynolds et al., 2007). The expansion of the salt-rich rough crust in 2006 can be related to the relatively dry period (Fig. 5), but also to changes in the groundwater levels beneath the playa. There is often

dynamic equilibrium in playas between geomorphic processes and groundwater levels for those areas in which the groundwater involved in their sediment formation. Relations between groundwater levels and surface types have been demonstrated by Reynolds et al. (2007) for a wet playa, Franklyn Lake, Mojave Desert, CA. It is reasonable to link the sediment distribution in November 2003 to the recorded gradient of increasing depth to groundwater in southwest–northeast direction (see Section 3), so that the green pixels in the west side are associated with near-surface water and the black and blue pixels with the capillary-fringe zone. A spectral distinction between different clayey silt-rich surfaces unfortunately was not made in this study, thus the west and northeast sides of Soda Lake appear as green pixels in the RGB images. However, alteration in green and red pixels at the northeast side may indicate deep groundwater levels and therefore low salt contents in the soil surface at this side of the playa compared to the clayey-silt surface at the west side. If the surface types in wet playas do reflect the groundwater, the expansion of the salt-rich rough crust (blue pixels) toward west in 2006 images may point on decreasing in the groundwater level and/or changes in the brine type between 2004 and 2006. Nonetheless, alteration in surface sediments affect the surface vulnerability to wind erosion, in which, for example, the resistance of salt-rich rough crust is higher than that of loose efflorescent salts cover (e.g., Reynolds et al., 2007). In this context, it is reasonable to assume that in July 2006 the playa surface was less sensitive to wind erosion.

8. Conclusions

The approach employed here, involving time-series of multispectral ASTER TIR data and spectral mixture analysis, has shown that, despite the complexity of a wet playa surface, major surface sediments can be identified and their spatial relationships over time can be modeled. More specifically, the multispectral Level-2 (L2) emissivity (AST_05) ASTER product can be used successfully to study surface sediments due to its ability to distinguish the emissivity spectral features of common

clastic and chemical minerals. Secondly, the variation of ASTER filtered spectra in discrimination of surface minerals emphasizes the use of image endmembers as reference spectra in spectral mixture analysis. Thirdly, the ASTER spectral mixtures of fine-grained surface with abundant chemical precipitation such as halite and thenardite may be closely linked to the development level (surface dehydration stage) of the efflorescent salts in order to be identified. Fourthly, the use of a spectral library constructed from representative multitemporal spectra of modern depositional environments allows minimization of RMS errors and comparison among the modeled spectra; however, an uncertainty regarding the differentiation between clayey silt-rich crusts (green pixels, Fig. 12) remains in this study. Finally, using fractional abundance images appears to be a useful method for spatially-detailed assessment of the surface sediments in dynamic landforms such as wet playas. The approach utilized in this study is appropriate to monitor surface sediments in other depositional environments, although they may vary greatly in their physical settings. Once the major spectra that represent the land surfaces over time have been constructed, it is possible to detect current changes by variations in spectral features of the image endmembers extracted from the new data set and/or directly by the spectral mixture analysis.

It revealed from the fractional abundance images that the surface sediments in Soda Lake and their spatial relationships can be changed significantly after heavy rainfall (image 2005), but also during a relatively dry period (image 2006), suggesting that the mosaic-like pattern of the surface sediments in such environments may reflect the potential for wind erosion and dust emission at a certain time. Continuous monitoring of these environments synthesized with climatologic and soil data may provide insights into their responses to hydrologic and geomorphic process and therefore dust emissions.

Acknowledgments

This study was supported in part by NASA grant NAG5-13730. CLIM-MET data courtesy of the U.S. Geological Survey. We thank Stephen Scheidt (University of Pittsburgh) for his assistance with the deconvolution algorithm. We also thank two anonymous referees for their useful comments.

References

- Adams, J. B., & Gillespie, A. R. (2006). *Remote sensing of landscapes with Spectral Images: A physical modeling approach*. New York: Cambridge Univ. Press 362 pp.
- Bandfield, J. L. (2002). Global mineral distributions on Mars. *Journal of Geophysical Research*, 107(E6), 5042. doi:10.1029/2001JE001510.
- Blount, G., Smith, M. O., Adams, J. B., Greeley, R., & Christensen, P. R. (1990). Regional aeolian dynamics and sand mixing in the Gran Desierto: Evidence from Landsat Thematic Mapper images. *Journal of Geophysical Research*, 95, 15463–15482.
- Brown, W. J., (1989). The Late Quaternary stratigraphy, paleohydrology, and geomorphology of fluvial Lake Mojave, Silver Lake and Soda Lake basins, Southern California. Master's thesis: Albuquerque, NM, University of New Mexico, 266 p.
- Bryant, R. G. (1996). Validated linear mixture modelling of Landsat TM data for mapping evaporite minerals on a playa surface. *International Journal of Remote Sensing*, 17, 315–330.
- Christensen, P. R., Bandfield, J. L., Hamilton, V. E., Howard, D. A., Lane, M. D., Piatek, J. L., et al. (2000). A thermal emission spectral library of rock-forming minerals. *Journal of Geophysical Research*, 105, 9735–9739.
- Clark, R. N. (1999). Spectroscopy of rocks and minerals and principles of spectroscopy. In A. N. Renz (Ed.), *Remote sensing for the earth sciences: Manual of remote sensing*, Vol. 3 (3rd edition) (pp. 3–58). New York: John Wiley and Sons.
- Crowley, J. K. (1993). Mapping playa evaporite minerals with AVIRIS data: A first report from Death Valley, CA. *Remote Sensing of Environment*, 44, 337–356.
- Crowley, J. K., & Hook, S. J. (1996). Mapping playa evaporite minerals and associated sediments in Death Valley, CA, with multispectral thermal infrared images. *Journal of Geophysical Research*, 101(B1), 643–660.
- Enzel, Y., Wells, S. G., & Lancaster, N. (2003). Late Pleistocene lakes along the Mojave River, southeast California. In Y. Enzel, S. G. Wells, & N. Lancaster (Eds.), *Paleoenvironments and paleohydrology of the Mojave and southern Great Basin deserts*, Vol. 368. (pp. 61–78): Geological Society of America Special Paper.
- Eugster, H. P., & Hardie, L. A. (1978). Saline lakes. In A. Lerman (Ed.), *Lakes: Chemistry, geology, physics* (pp. 237–293). New York: Springer-Verlag.
- Gillespie, A. (1992). Spectral mixture analysis of multispectral thermal infrared images. *Remote Sensing of Environment*, 42, 137–145.
- Gillespie, A., Cothorn, J. S., Rokugawa, S., Matsunaga, T., Hook, S. J., & Kahle, A. B. (1998). A temperature and emissivity algorithm for Advanced Spaceborne Thermal Emission and Reflection Radiometer (ASTER) images. *IEEE Transactions on Geoscience and Remote Sensing*, 36, 1116–1126.
- Gillespie, A. R., Kahle, A. B., & Walker, R. E. (1986). Color enhancement of highly correlated images: I. Decorrelation and HSI contrast stretches. *Remote Sensing of Environment*, 20, 209–235.
- Gillette, D. A. (1999). A qualitative geophysical explanation for “hot spot” dust emitting source regions. *Contributions to Atmospheric Physics*, 72, 67–77.
- Goudie, A. S., & Middleton, N. J. (2006). *Desert dust in the global system*. NY: Springer.
- Gruninger, J., Ratkowski, A. J., & Hoke, M. L. (2004, April). “The Sequential Maximum Angle Convex Cone (SMACC) endmember model”. *Proceedings SPIE, algorithms for multi-spectral and hyper-spectral and ultraviolet imagery*, Vol. 5425-1. Orlando FL.
- Hunt, G. R. (1980). Electromagnetic radiation: The communication link in remote sensing. In B. S. Siegal & A.R. amd Gillespie (Eds.), *Remote sensing in geology* (pp. 5–45). New York: John Wiley.
- Kampf, S. K., & Tyler, S. W. (2006). Spatial characterization of land surface energy fluxes and uncertainty estimation at the Salar de Atacama, Northern Chile. *Advances in Water Resources*, 29, 336–354.
- Kerr, P. F., & Langer, A. M. (1965). Mineralogical features of Mojave Desert playa crusts. In J. T. Neal (Ed.), *Geology, mineralogy, and hydrology of U.S. playas* Cambridge Research Laboratory Environmental Research Paper, Vol. 96. (pp. 31–72).
- Kruse, F. A., Lefkoff, A. B., Boardman, J. B., Heidebrecht, K. B., Shapiro, A. T., Barloon, P. J., et al. (1993). The Spectral Image Processing System (SIPS) – Interactive visualization and analysis of imaging spectrometer data. *Remote Sensing of Environment*, 44, 145–163.
- Lane, M. D., & Christensen, P. R. (1997). Thermal infrared emission spectroscopy of anhydrous carbonates. *Journal of Geophysical Research*, 102, 25581–25592.
- Michalski, J. R., Reynolds, S. J., Sharp, T. G., & Christensen, P. R. (2004). Thermal infrared analysis of weathered granitic rock compositions in the Sacaton Mountains, Arizona: Implications for petrologic classifications from thermal infrared remote-sensing data. *Journal of Geophysical Research*, 109, E03007. doi:10.1029/2003JE002197.
- Millington, A. C., Drake, N. A., Townshend, J. R. G., Quarmby, N. A., Settle, J. J., & Reading, A. J. (1989). Monitoring salt playa dynamics using Thematic Mapper data. *IEEE Transactions on Geoscience and Remote Sensing*, 27, 754–761.
- Neal, J. T. (1968). Playa surface changes at Harper Lake, California: 1962–1967. In J. T. Neal (Ed.), *Playa surface morphology: Miscellaneous investigations* Cambridge Research Laboratory Environmental Research Paper, Vol. 283. (pp. 5–30).
- Prospero, J. M., Ginoux, P., Torres, O., Nicholson, S. E., & Gill, T. E. (2002). Environmental characterization of global sources of atmospheric soil dust identified with the Nimbus-7 Total Ozone Mapping Spectrometer (TOMS) absorbing aerosol product. *Reviews of Geophysics*, 40, 1–31.
- Ramsey, M. S., & Christensen, P. R. (1998). Mineral abundance determination: Quantitative deconvolution of thermal emission spectra. *Journal of Geophysical Research*, 103, 577–596.
- Ramsey, M. S., Christensen, P. R., Lancaster, N., & Howard, D. A. (1999). Identification of sand sources and transport pathways at the Kelso Dunes, California using thermal infrared remote sensing. *Geological Society of America Bulletin*, 111, 646–662.
- Reheis, M. (2006). A 16-year record of eolian dust in Southern Nevada and California, USA: Controls on dust generation and accumulation. *Journal of Arid Environments*, 67, 487–520.
- Reheis, M., & Kihl, R. (1995). Dust deposition in southern Nevada and California, 1984–1989: Relations to climate, source area, and source lithology. *Journal of Geophysical Research*, 10, 8893–8918.
- Reynolds, R. L., Yount, J. C., Reheis, M., Goldstein, H., Chavez, P., Jr., Fulton, R., et al. (2007). Dust emission from wet and dry playas in the Mojave Desert, USA. *Earth Surface Processes and Landforms*, 32, 1811–1827.
- Rezaei, M. H., & Saghafi, M. (2006). A change-detection application on the evolution of Kahak playa (South Khorasan province, Iran). *Environmental Geology*, 51, 565–579.
- Rosen, M. R. (1994). The importance of groundwater in playas: A review of playa classifications and the sedimentology and hydrology of playas. In M. R. Rosen (Ed.), *Paleoclimate and basin evolution of playa systems*, Vol. 289. (pp. 1–18): Geological Society of America Special Paper.
- Rowan, L. C., & Mars, J. C. (2003). Lithologic mapping in the Mountain Pass, California area using Advanced Spaceborne Thermal Emission and Reflection Radiometer (ASTER) data. *Remote Sensing of Environment*, 84, 350–366.
- Rowan, L. C., Mars, J. C., & Simpson, C. J. (2005). Lithologic mapping of the Mordor, NT, Australia ultramafic complex by using the Advanced Spaceborne Thermal Emission and Reflection Radiometer (ASTER). *Remote Sensing of Environment*, 99, 105–126.
- Salisbury, J. W., & Wald, A. (1992). The role of volume scattering in reducing spectral contrast of reststrahlen bands in spectra of powdered minerals. *Icarus*, 96, 121–128.
- Vaughan, R. G., Hook, S. J., Calvin, W. M., & Taranik, J. V. (2005). Surface mineral mapping at Steamboat Springs, Nevada, USA, with multi-wavelength thermal infrared images. *Remote Sensing of Environment*, 99, 140–158.
- Washington, R., Todd, M. C., Lizzano, G., Tegen, I., Flamant, C., Koren, I., et al. (2006). Links between topography, wind, deflation, lakes and dust: The case of the Bodélé Depression, Chad. *Geophysical Research Letters*, 33, L09401. doi:10.1029/2006GL025827.
- Wells, S. G., Brown, W. J., Enzel, Y., Anderson, R. Y., & McFadden, L. D. (2003). Late Quaternary geology and paleohydrology of pluvial Lake Mojave, southern California. In Y. Enzel, S. G. Wells, & N. Lancaster (Eds.), *Paleoenvironments and paleohydrology of the Mojave and southern Great Basin deserts*, Vol. 368. (pp. 79–114): Geological Society of America Special Paper.
- Yamaguchi, Y., Kahle, A. B., Tsu, H., Kawakami, T., & Pniel, M. (1998). Overview of Advanced Spaceborne Thermal Emission and Reflection Radiometer (ASTER). *IEEE Transactions on Geoscience and Remote Sensing*, 36, 1062–1071.